Journal of Computational Physics **148,** 169–198 (1999)
Article ID jcph.1998.6116, available online at http://www.idealibrary.com on IDEAL®

A Lagrangian Vorticity Method for Two-Phase Particulate Flows with Two-Way Phase Coupling

H. Chen and J. S. Marshall

Department of Mechanical Engineering and Iowa Institute of Hydraulic Research, The University of Iowa, Iowa City, Iowa 52242

Received August 20, 1997; revised September 27, 1998

A Lagrangian vorticity-based method is presented for simulating two-way phase interaction in a two-phase flow with heavy particles. The flow is computed by solving the vorticity transport equation, including the particle-induced vorticity source, and the mass conservation equation for particle concentration on separate sets of fluid control points and particle control points, respectively. The fluid control points are advected with the local fluid velocity, plus a diffusion velocity for viscous problems to account for the spread of the vorticity support via diffusion, while the particle control points are advected by solution of the Lagrangian particle momentum equation. The particle concentration and vorticity transport equations are evaluated using volume-averaged particle velocity and contact force fields, obtained by a weighted average over nearby particle control points. One novel feature of the numerical method is the scheme for calculation of the particle-induced vorticity source using a "moving least-square" differentiation scheme across the two sets of control points. Another feature of the method is its ability to absorb the vorticity generated by particle forces through an adaptive scheme for generation of new fluid control points. Test calculations with a vortex patch filled with particles show that the numerical results compare well with the results obtained both by a traditional finite-difference method and by an asymptotic approximation valid for small Stokes numbers. Other features of the numerical method are demonstrated for calculations involving a particle cloud falling under gravity and a two-phase mixing layer flow.

Key Words: two-phase flow; vortex methods.

1. INTRODUCTION

Two-phase flows involving solid particles or droplets in gases or bubbles or sediment in liquids have been subject to intensive study for decades due to their wide range of applications in industrial and environmental processes. Much of the previous work has

0021-9991/99 $30.00

focused on investigation of particle dynamics and dispersion [1–9]. These studies typically employ the *one-way coupling* approximation, in which the influence of the particles on the motion of the carrier fluid is assumed to be negligible. While the one-way coupling approximation is simple to implement, it is generally valid only for flows with small particle mass concentrations [10].

Even for flows with small average particle mass fraction, local values of the particle mass concentration may increase significantly above the average value due to the particle inertia bias. For instance, in a direct numerical simulation of isotropic turbulence, Squires and Eaton [4] found that preferential collection of particles in regions of low vorticity and high strain rate causes the instantaneous value of the particle concentration to increase in certain regions of the flow by as much as 25 times the mean value. Studies of particle dispersion in free shear flows [1–3, 5–7, 9] similarly show that the particles are expelled from the vortex centers and accumulate in thin bands at the edges of the vortex structures. The above observations suggest that even for low average particle mass concentration, the one-way coupling assumption may be invalid in certain regions of the flow.

There are two competing methods commonly used to model two-phase flows with significant two-way interaction between the fluid and particle phases. In the *two-fluid approach*, the basic variables are continuous fields that can be associated with averages over the individual particles, and include the average particle and fluid velocity fields and the particle mass concentration. Evolution equations for particle mass concentration and fluid and particle momentum are similarly obtained by averaging the mass and momentum balances over a set of small control volumes spanning the flow [11, 12]. The averaged particle momentum equation contains an additional Reynolds-stress-type term, given by the average of the product of the fluctuating particle velocities, for which a closure model must be prescribed. The common procedure [13] is to adopt a Boussinesq-type model, in which this term is replaced by the product of the symmetric part of the average particle velocity gradient and a proportionality coefficient, often called the "particle viscosity." Another area requiring modeling in the two-fluid approach is the boundary slip for the average particle velocity at the surface of a solid body. As discussed in the recent review by Crowe *et al.* [13], models for the slip boundary condition of the average particle velocity are diverse and pose some fundamental difficulties.

The *Lagrangian approach* avoids the necessity of introducing closure models for the averaged variables by directly evolving a set of "representative" particles using the momentum equation for an individual particle. The individual particle momentum equation requires only relatively well-established expressions for the force acting on a single spherical particle moving in the fluid, where in a dilute flow the effect of other particles is neglected. The boundary conditions at a solid surface can similarly be handled using well-established expressions [14] for the elastic and partially elastic rebound of an individual particle from a plane surface.

As noted in recent review articles by Stock [15] and Crowe *et al.* [13], the Lagrangian approach is not without shortcomings. In particular, the methods typically used in the Lagrangian approach to compute the particle concentration field (which is required for many applications) and the particle-induced force on the fluid are quite inefficient. The particle concentration can be estimated by counting the number of particle control points in each fluid grid cell [16]. The particle force on the fluid can be obtained by evaluating the change in momentum of the particle control points as they exit and enter the grid cells [17, 18]. In order for the particle concentration field and the particle-induced fluid force to be smoothly

varying in space, the number of Lagrangian particle control points must be at least an order of magnitude larger than the number of fluid grid cells. It is typical in Lagrangian methods to let each computational particle represent a "cluster" of actual particles that are carried along with the computational particles. In most existing Lagrangian methods the number of particles in each cluster is fixed during the computation, although exchange of particles between the computational particles may be desirable in cases where the particle positions become very deformed from their initial ordering or as a model for particle dispersion from subgrid-scale fluctuations in turbulent flows.

For certain categories of two-phase flows, such as bluff body wakes and mixing layers, the use of vortex methods for fluid flow simulation offers a number of advantages compared to more traditional approaches based on the velocity–pressure formulation on a fixed grid. Some of the advantages of vortex methods are evident from the following observations: (i) fluid control points need only be introduced in regions where there is significant vorticity; (ii) external flows can be solved without truncation to a finite domain; (iii) there is little or no numerical dissipation; (iv) the vorticity–velocity formulation does not depend on pressure, and therefore it requires no iteration to satisfy the continuity equation and avoids specification of pressure boundary conditions; (v) vortex methods are naturally highly adaptive, since control points are carried to regions of high vorticity by the flow. Vortex methods have previously been used for two-phase flow calculations by a number of researchers for studies of particle dispersion in cases where the one-way coupling approximation applies [1–3, 5–7]. However, because the method described above to compute two-way coupling with the Lagrangian particle approach relies on the existence of a grid covering the flow field, vortex methods have not previously been employed for cases where there exists significant modification of the fluid flow by the particles.

The present paper introduces a new method for computation of two-way coupling in particulate two-phase flows in the context of a Lagrangian vortex method. The method utilizes two sets of control points, one associated with the fluid vorticity field and the other with the particle mass concentration. The vorticity transport equation is evolved on the fluid control points, while the mass conservation equation for the dispersed phase is evolved on the particle control points. The fluid control points are advected with the local fluid velocity, plus a "diffusion velocity" for viscous problems [19, 20] to account for the spread of the vorticity support via diffusion. The particle control points are advected by solution of the particle momentum equation for individual "representative" particles. A moving averaging procedure is used to compute the volume-averaged particle velocity and contact force at each computational particle control point, where the averaged fields are used in solution of the particle concentration and vorticity transport equations. Novel features of the solution method include a scheme for numerical differentiation across two sets of irregularly spaced control points and an adaptive scheme for generation of new fluid control points to absorb the vorticity generated by particle forces.

The proposed two-phase flow solution method combines some of the best attributes of the two-fluid and Lagrangian approaches. Use of the Lagrangian version of the individual particle momentum equation avoids the necessity of introducing a closure model for the Reynolds-stress term in the average particle momentum equation. Solution of the particle concentration equation on each particle control point yields a smooth concentration field without an excessive number of particle control points. The effect of the particles on the fluid flow is computed by differentiating directly over the Lagrangian control points, without requiring the presence of a grid spanning the flow. The proposed method is an alternative to

the sometimes controversial [10] clustering method commonly employed for prediction of two-way coupling with the Lagrangian particle advection approach. While the two-phase flow solution method is presented in the current paper in the context of a Lagrangian vortex method, it can be implemented in conjunction with any standard numerical method for solution of the continuous phase momentum equation.

The governing equations for both fluid and particulate phases are given in Section 2. Section 3 describes the numerical algorithms used to solve for the fluid and particle motion, including the particle-induced vorticity source. In Section 4, computational results are presented for vorticity modification due to particles in a vortex patch flow, and the error incurred by variation of different numerical parameters is evaluated in comparison to results of a one-dimensional (axisymmetric) finite-difference method and an asymptotic method for low Stokes numbers. Section 5 demonstrates the ability of the numerical method to resolve the particle-induced vorticity in a flow where the particles move a large distance from the initial fluid control points. Computations of particle–fluid two-way interaction in a mixing-layer flow are given in Section 6. Concluding remarks are given in Section 7.

2. GOVERNING EQUATIONS

The current study employs the following assumptions: (i) the particle volume fraction is sufficiently small that particle–particle interactions are negligible; (ii) particles are sufficiently small compared with the length scales of fluid motion that they can be treated as point forces and the particle wake effects can be neglected; (iii) all particles are spheres of the same diameter d_p; (iv) particle material density is much larger than that of the fluid; (v) the carrier fluid is incompressible and the flow is two dimensional. The restriction to two-dimensional flows is not necessary, and the method has been implemented for both two- and three-dimensional flows, but it simplifies the presentation in the present paper.

The particle momentum equation for a small, rigid sphere in a nonuniform flow is given by Maxey and Riley [21]. For flow in which the material density ρ_p is much greater than the density ρ_f of the fluid phase, the forces due to ambient pressure gradient and added mass, as well as the Basset history force, are negligible. Similarly, the small particle lift force that arises in the presence of a background vorticity field [22–25] is typically neglected in most particulate flow simulations. For simplicity, we omit these small forces in the following equations and concentrate on the drag and gravity forces, although the computational method is unchanged if these other forces are added. With this simplification, the momentum equation for an individual particle can be written in dimensionless form as

$$\frac{d\vec{\mathbf{v}}}{dt} = \vec{\mathbf{f}} + \frac{1}{\mathrm{Fr}^2}\vec{\mathbf{e}}_g, \tag{1}$$

where $\vec{\mathbf{v}}$ is the particle velocity and d/dt denotes the time derivative following an individual particle, such that for any quantity f,

$$\frac{df}{dt} \equiv \frac{\partial f}{\partial t} + \vec{\mathbf{v}} \cdot \vec{\nabla} f. \tag{2}$$

The Froude number Fr is defined by $\mathrm{Fr} \equiv U/\sqrt{gL}$, where g is the gravitational acceleration and L and U are characteristic length and velocity scales of the fluid flow used to write the variables in dimensionless form. The symbol $\vec{\mathbf{e}}_g$ in (1) denotes the unit vector in the

direction of gravity, and $\vec{\mathbf{f}}$ denotes the contact force acting on a single particle divided by the particle mass. Considering drag as the only contact force, the dimensionless contact force can be expressed as [26]

$$\vec{\mathbf{f}} = -\frac{1}{\mathrm{St}}\left(1 + 0.15\,\mathrm{Re}_p^{0.687}\right)(\vec{\mathbf{v}} - \vec{\mathbf{u}}), \tag{3}$$

for values of the particle Reynolds number, $\mathrm{Re}_p \equiv \rho_f |\vec{\mathbf{v}} - \vec{\mathbf{u}}| d_p/\mu$, less than about 800. In (3), $\vec{\mathbf{u}}$ denotes the fluid velocity evaluated at the particle position and St is the Stokes number, defined as the ratio of particle aerodynamic response time to the characteristic time of the carrier fluid motion. The expression $\mathrm{St} \equiv \rho_p d_p^2 U/18\ \mu \mathrm{L}$ for Stokes number used in writing (3) is appropriate for small values of the particle Reynolds number.

The basis of the two-fluid model is the volume averaging procedure. We let $W(\vec{\mathbf{x}} - \vec{\mathbf{x}}_n)$ denote a "localization" function, which decays rapidly away from the point $\vec{\mathbf{x}}_n$. A radial length scale α_n is associated with $W(\vec{\mathbf{x}} - \vec{\mathbf{x}}_n)$, which is assumed to be sufficiently small that the "mean" flow is not sensitive to variation of α_n . If q denotes any instantaneous variable associated with the particulate or fluid phase, then the volume average $\langle q \rangle$ of q in the vicinity of $\vec{\mathbf{x}}_n$ is defined by

$$\langle q \rangle \equiv \frac{\int_V q(\vec{\mathbf{x}}) W(\vec{\mathbf{x}} - \vec{\mathbf{x}}_n)\, d\nu}{\int_V W(\vec{\mathbf{x}} - \vec{\mathbf{x}}_n)\, d\nu}, \tag{4}$$

where V is the total region occupied by the flow. A common example is to set $W(\vec{\mathbf{x}} - \vec{\mathbf{x}}_n)$ equal to unity within some small region V_n surrounding $\vec{\mathbf{x}}_n$ and equal to zero outside of this region.

A variable $a(\vec{\mathbf{x}}, t)$ is introduced that has the value unity within the particles and the value zero outside of the particles. With this notation, the particle mass concentration is given by the ratio of the particle mass to the total mixture volume, or $\rho_p \langle a \rangle$. The dimensionless particle concentration $c(\vec{\mathbf{x}}, t)$ is defined by $c = (\rho_p/\rho_f)\langle a \rangle$. The average particle velocity field $\vec{\mathbf{V}}(\vec{\mathbf{x}}, t)$ and the average particle contact force $\vec{\mathbf{F}}(\vec{\mathbf{x}}, t)$ are defined by

$$\vec{\mathbf{V}} \equiv \langle a\vec{\mathbf{v}} \rangle / \langle a \rangle, \qquad \vec{\mathbf{F}} \equiv \langle a\vec{\mathbf{f}} \rangle / \langle a \rangle. \tag{5}$$

Application of the volume averaging procedure to the particle mass balance yields an equation for particle mass concentration [12] as

$$\frac{\partial c}{\partial t} + \vec{\nabla} \cdot (c\vec{\mathbf{V}}) = 0. \tag{6}$$

Rewriting of (6) using the material derivative d/dt following an individual particle, defined in (2), gives

$$\frac{dc}{dt} + c\vec{\nabla} \cdot \vec{\mathbf{V}} + (\vec{\mathbf{V}} - \vec{\mathbf{v}}) \cdot \vec{\nabla} c = 0. \tag{7}$$

Unlike the fluid velocity, the average particle velocity field $\vec{\mathbf{V}}$ is not divergence free, even in an incompressible flow, due to the effect of particle dispersion.

In writing the governing equations for the fluid flow, the particles are treated as point forces, where the particle contact force is volume averaged to yield the particle-induced

body force acting on the flow. This body force is nonconservative, such that the curl of this force yields a source term in the vorticity transport equation [13]. Restricting attention to two-dimensional flows, the vorticity transport equation becomes

$$\frac{D\omega}{Dt} = \frac{1}{\mathrm{Re}}\nabla^2\omega - \nabla \times (c\vec{\mathbf{F}})\Big|_k, \tag{8}$$

where $D/Dt \equiv \partial/\partial t + \vec{\mathbf{u}} \cdot \nabla$ is the material derivative following the fluid motion, ω is the vorticity magnitude, and $\mathrm{Re} \equiv UL/\nu$ is the flow Reynolds number. The form of the last term in (8) is derived in Appendix A, and the subscript k attached to this term denotes the component of the curl normal to the plane of the flow.

Using the Helmholtz decomposition, the fluid velocity $\vec{\mathbf{u}}$ can be written as the sum of an irrotational vector, which is either harmonic or induced by the fluid dilatation, and a solenoidal vector, which is induced by the vorticity. In an unbounded incompressible fluid with zero velocity at infinity, the first of these parts vanishes and the fluid velocity is given by the Biot–Savart integral

$$\vec{\mathbf{u}}(\vec{\mathbf{x}}, t) = -\frac{1}{2\pi}\int_A \frac{(\vec{\mathbf{x}} - \vec{\mathbf{x}}') \times \vec{\mathbf{k}}}{|\vec{\mathbf{x}} - \vec{\mathbf{x}}'|^2}\omega(\vec{\mathbf{x}}', t)\, da', \tag{9}$$

where $\vec{\mathbf{k}}$ is the unit normal to the plane of motion and the area integration is over the primed coordinate.

3. COMPUTATIONAL APPROACH

3.1. *Fluid Flow Field*

The fluid flow is evaluated by solution of the vorticity transport equation (8), together with the Biot–Savart integral (9) for the fluid velocity, using a Lagrangian vorticity-based method in which the vorticity evolution is followed on a set of N "fluid" control points with locations $\vec{\mathbf{x}}_n(t) = x_n\vec{\mathbf{e}}_x + y_n\vec{\mathbf{e}}_y$, where $n \in (1, N)$. In inviscid flow, the fluid control points are advected by the local fluid velocity $\vec{\mathbf{u}}(\vec{\mathbf{x}}_n, t)$. In a viscous flow, the fluid control points are advected by the sum of the local fluid velocity $\vec{\mathbf{u}}(\vec{\mathbf{x}}_n, t)$ and a "diffusion velocity" $\vec{\mathbf{u}}_d(\vec{\mathbf{x}}_n, t)$, given by $\vec{\mathbf{u}}_d(\vec{\mathbf{x}}_n, t) = -(1/\mathrm{Re})(\vec{\nabla}\omega/\omega)$, so that

$$\frac{D\vec{\mathbf{x}}_n}{Dt} = \vec{\mathbf{u}}(\vec{\mathbf{x}}_n, t) + \vec{\mathbf{u}}_d(\vec{\mathbf{x}}_n, t). \tag{10}$$

The diffusion velocity has the property that the circulation is invariant about any circuit that is advected with the sum of the local fluid velocity and the diffusion velocity [20].

Biot–Savart integral. In order to obtain the velocity field induced by the Biot–Savart integral (9), the vorticity is interpolated by a set of N overlapping, smooth elements centered at each of the N control points [27–31]:

$$\omega(\vec{\mathbf{x}}, t) = \sum_{n=1}^{N} \Omega_n(t)\psi_{\delta_n}(\vec{\mathbf{x}} - \vec{\mathbf{x}}_n). \tag{11}$$

The element weighting function $\psi_{\delta_n}(\vec{\mathbf{x}} - \vec{\mathbf{x}}_n)$, normalized so that its integral over all space is unity, determines the vorticity distribution of the element centered at $\vec{\mathbf{x}}_n$ with the length scale

δ_n (called the element "radius"). For the current study, the weighting function is chosen as a Gaussian

$$\psi_{\delta_n}(\vec{\mathbf{x}} - \vec{\mathbf{x}}_n) = \frac{1}{\pi \delta_n^2} \exp\left(-|\vec{\mathbf{x}} - \vec{\mathbf{x}}_n|^2 / \delta_n^2\right). \tag{12}$$

The element amplitude Ω_n represents the integral of the vorticity associated with element n over all space. Substituting (11) into (9) and integrating yields an expression for fluid velocity as

$$\vec{\mathbf{u}}(\vec{\mathbf{x}}, t) = \frac{1}{2\pi} \sum_{n=1}^{N} \frac{\Omega_n}{r^2} \left[1 - \exp\left(-r^2 / \delta_n^2\right)\right] [(\vec{\mathbf{x}} - \vec{\mathbf{x}}_n) \times \vec{\mathbf{k}}], \tag{13}$$

where $r \equiv |\vec{\mathbf{x}} - \vec{\mathbf{x}}_n|$.

The fluid velocity at any point is thus obtained as a sum over all fluid control points, provided that the amplitude Ω_n is known. Two types of schemes have been used in the literature for calculating the element amplitudes Ω_n from (11) for the given vorticity values ω_n at the control points. In the standard vortex blob method (e.g., Leonard [27, 28]), the element amplitude is set equal to an initial amount of vorticity $h_n^2 \omega_n$, where h_n^2 is a constant area which is associated with each element. The vorticity ω_n at each control point is evolved according to the vorticity transport equation (3). Beale [32] pointed out that as the control points move relative to each other, the amount of element overlap at any one control point due to its neighboring control points can vary considerably, unless the ratio h_n/δ_n is very small. This change in element overlap can lead to a substantial increase in error for both the velocity and vorticity fields after a sufficiently long time.

An alternative method for determination of element amplitude (which we call the "vorticity collocation" method) is proposed by Beale [32] and refined by Marshall and Grant [33, 34], in which the element amplitudes are fit to the computed vorticity field at every time step. Evaluating the vorticity representation (11) at the locations of the fluid control points results in an $N \times N$ matrix equation for the element amplitudes Ω_n. This matrix equation is ill conditioned, such that if the vorticity values ω_n at the control points are set based on a smooth vorticity field, the resulting amplitude values Ω_n from exact solution of the matrix equation oscillate wildly. Beale [32] solved this matrix equation using an exact iterative procedure, and found that if only a few iterations are used, the long-time error in the standard vortex method could be substantially reduced. However, Beale's iterative procedure is not well behaved since it converges to an exact solution of the matrix equation, such that after a sufficient number of iterations it also produces noisy results. Marshall and Grant [33] proposed an approximate iterative procedure, which filters out the high wave number noise in the amplitude distribution, where the element amplitude is temporarily assumed to be uniform over a set of elements $Q(\ell)$ located in the neighborhood of element ℓ. The matrix equation for element amplitude thus yields the iteration procedure

$$\omega_\ell = \Omega_\ell^{(j+1)} \sum_{n \in Q(\ell)} \psi_{\delta_n}(\vec{\mathbf{x}}_\ell - \vec{\mathbf{x}}_n) + \sum_{n \in P(\ell)} \Omega_n^{(j)} \psi_{\delta_n}(\vec{\mathbf{x}}_\ell - \vec{\mathbf{x}}_n), \tag{14}$$

where $P(\ell)$ is the complement of $Q(\ell)$ and j is the iteration index. This procedure converges very quickly with an error of order $\delta^2 \nabla^2 \omega$, where the element radius δ is on the order of the distance between neighboring control points, and the procedure acts to smooth out vorticity fluctuations occurring on a scale much smaller than δ.

Particle-induced vorticity source. In computing the particle-induced vorticity source in (8), it is necessary to differentiate the product $c\vec{\mathbf{F}}$, whose value is known on the set of M "particle" control points with locations $\vec{\xi}_m(t) = \xi_m \vec{\mathbf{e}}_x + \eta_m \vec{\mathbf{e}}_y$, where $m \in (1, M)$. The value of this derivative is required to be known on the fluid control points $\vec{\mathbf{x}}_n$, where $n \in (1, N)$. Both the particle and fluid control points are irregularly spaced and are not connected by any grid structure. Differentiation of some function $g(\vec{\mathbf{x}})$ is performed by a "moving least-square" method, in which a polynomial is fit to the value of $g(\vec{\mathbf{x}})$ on particle control points lying in a small region close to a given fluid control point at which the derivative is desired. For a nominally second-order accurate method, a quadratic polynomial is used for local interpolation of $g(\vec{\mathbf{x}})$ of the form

$$q_n(x, y) \equiv g_n + A_n\left(\frac{x - x_n}{\delta_n}\right) + B_n\left(\frac{y - y_n}{\delta_n}\right) + C_n\left(\frac{x - x_n}{\delta_n}\right)\left(\frac{y - y_n}{\delta_n}\right) + D_n\left(\frac{x - x_n}{\delta_n}\right)^2 + E_n\left(\frac{y - y_n}{\delta_n}\right)^2. \tag{15}$$

To obtain the coefficients in (15), a locally weighted least-square error criterion is employed, in which an error ε_n is defined by

$$\varepsilon_n \equiv \sum_{m=1}^{M} L_{mn}[g_m - q_n(\xi_m, \eta_m)]^2, \tag{16}$$

where m and n are indices over the particle and fluid control points, respectively. The "localization" function L_{mn} serves to select the particle control points close to the fluid control point n and is chosen as

$$L_{mn} = \exp\left[-\frac{(\xi_m - x_n)^2 + (\eta_m - y_n)^2}{\delta_n^2}\right]. \tag{17}$$

Extremizing ε_n with respect to these coefficients, as well as with respect to g_m in (15), yields a system of six linear equations for g_m and the five coefficients $A_n, \ldots, E_n$, given by

$$\sum_{m=1}^{M} L_{mn}\left(\frac{\xi_m - x_n}{\delta_n}\right)^i \left(\frac{\eta_m - y_n}{\delta_n}\right)^j [g_m - q_n(\xi_m, \eta_m)] = 0, \tag{18}$$

where the exponents i and j satisfy $(i, j) \in (0, 1, 2)$ and $0 < i + j < 3$. Once the coefficients are obtained by solution of the 6×6 matrix equation at each fluid control point, the derivatives at the fluid control points are approximated by differentiation of the quadratic fit (15).

In computing the particle-induced vorticity source, a quadratic polynomial must be fit to the value of $c\vec{\mathbf{F}}$ on a set of neighboring particle control points for each fluid control point. For a flow system that contains N fluid control points and M particle control points, this process would require $O(NM)$ operations, which is very time consuming for large N and M. To speed up this process, a list is stored identifying particle control points in the neighborhood of each fluid control point. The list is built by first sorting all the particle controls points into an adaptive tree-like box structure (see below for a detailed discussion on construction of the box structure) and then searching the nearest boxes.

It is noted that the "moving least-square" differentiation method reduces to the standard centered-difference method when the points are uniformly spaced and only nearest points are utilized in the fit. A similar differentiation method was used by Marshall and Grant [34] in simulating the viscous diffusion of vorticity. They showed that the moving least-square method is able to maintain high accuracy even for cases with very irregularly spaced points.

As noted previously in the Introduction, particles collect in regions with low or even no vorticity, such that the region covered by the particle and fluid control points may become widely separated in space. To better resolve the flow field, we employ an algorithm for addition of new fluid control points near the particle control point locations. In this algorithm, the particles are sorted into an adaptive tree-like box structure, which is initiated by sorting the particles into a uniform grid of "largest-size" boxes. If the number of particles in a box is greater than a prescribed upper limit N_L, the box is divided in two in the coordinate direction in which the distance between the two farthest particles in the box is the largest. The division is performed such that the two sub-boxes contain (almost) the same number of particles. This division process is repeated for each new generation of the offspring boxes until the number of particles in each box is less than N_L. The last generation of the division is called the "smallest-size" boxes. If a smallest-size box does not contain any fluid control points at the end of each time step, a new fluid control point is created at the centroid of particle locations in the box. The vorticity at this new control point is set by interpolation using the vorticity representation (11), after which the vorticity amplitudes for all fluid control points are refit.

Viscous diffusion of vorticity. In simulation of viscous flows, it is necessary to compute the Laplacian of vorticity $\nabla^2\omega$ in (3). Like the particle-induced vorticity source, in computing $\nabla^2\omega$ it is necessary to approximate derivatives of a function whose value is known on a set of irregularly spaced control points.

As noted at the beginning of this section, the fluid control points are advected in a viscous flow by the sum of the local fluid velocity $\vec{\mathbf{u}}(\vec{\mathbf{x}}_n, t)$ and the diffusion velocity $\vec{\mathbf{u}}_d(\vec{\mathbf{x}}_n, t)$. The rate of change of vorticity at a given fluid control point is given by a derivative $D_\nu\omega/Dt$, which is related to the material derivative $D\omega/Dt$ by

$$\frac{D_\nu\omega}{Dt} \equiv \frac{D\omega}{Dt} + \vec{\mathbf{u}}_d \cdot \nabla\omega. \tag{19}$$

The vorticity transport equation (8) can be rewritten in terms of this derivative as

$$\frac{D_\nu\omega}{Dt} = \frac{\omega}{\mathrm{Re}}\nabla^2(\ln|\omega|) - \vec{\nabla} \times (c\vec{\mathbf{F}})\Big|_k. \tag{20}$$

Following Marshall and Grant [34], $\ln|\omega|$ is computed on each fluid control point, and then the Laplacian of $\ln|\omega|$ is computed using a moving least-square differentiation method similar to that described above.

3.2. *Particle Dispersion*

The particle motion is represented by a set of Lagrangian particle control points $\vec{\xi}_m$, $m \in (1, M)$, where the particle velocity is obtained by solution of the particle momentum equation (2). The particle concentration is evolved on the particle control points by solution

of the particle mass conservation equation (7), where the moving least-square differentiation method is again used to approximate $\vec{\nabla} \cdot \vec{\mathbf{V}}$ and $\vec{\nabla} c$ in (7). Equations (2) and (7), as well as the vorticity transport equation (8) and the fluid control point advection equation (10), are advanced in time with a standard second-order predictor–corrector algorithm [35].

The average particle velocity $\vec{\mathbf{V}}$ and contact force $\vec{\mathbf{F}}$, used in (7)–(8), are computed at the location of each particle control point by a locally weighted average over nearby particle control points. We let W_{mn} denote a localization function, in the vicinity of a particle control point $\bar{\mathbf{y}}_n = \xi_n \vec{\mathbf{e}}_x + \eta_n \vec{\mathbf{e}}_y$, of the form

$$W_{mn} = \exp\left[-\frac{(\xi_m - \xi_n)^2 + (\eta_m - \eta_n)^2}{\alpha_n^2} \right], \tag{21}$$

where the radial length scale α_n is of the order of the distance between adjacent particle control points. The value of $\vec{\mathbf{V}}$ and $\vec{\mathbf{F}}$ at a particle control point $\vec{\xi}_m$ is then given by

$$\vec{\mathbf{V}}_m = \sum_{n=1}^{M} W_{mn} \vec{\mathbf{v}}_n \Bigg/ \sum_{n=1}^{M} W_{mn}, \qquad \vec{\mathbf{F}}_m = \sum_{n=1}^{M} W_{mn} \vec{\mathbf{f}}_n \Bigg/ \sum_{n=1}^{M} W_{mn}. \tag{22}$$

In solving the particle momentum equation (2), it is necessary to calculate the fluid velocity $\vec{\mathbf{u}}(\vec{\xi}_m, t)$ at the particle positions $\vec{\xi}_m$. This is commonly done in fixed grid studies by first evaluating the fluid velocities on a uniform grid of points and then interpolating to obtain the fluid velocities at the particle positions. However, in a vorticity-based method, the fluid velocity can be computed directly at the particle locations via solution of the Biot–Savart integral, as described in Section 3.1. In the current paper, we employ an adaptive acceleration method, which is an extension of that described by Greengard and Rohklin [36], for calculation of the fluid velocity at both the fluid control point positions $\vec{\mathbf{x}}_n$ and the particle control point positions $\vec{\xi}_m$ (see Appendix B for details). This acceleration method utilizes an adaptive tree-like box structure for the fluid control points similar to that described in Section 3.1 for the particles. The acceleration method enables a decrease in number of computations for a flow with N fluid control points and M particles from $O(N^2)$ to $O(N \ln N)$ for the velocity at fluid control points and from $O(MN)$ to $O(M \ln N)$ for the velocity at the particle control points.

4. VALIDATION TESTS

In this section, we examine the variation of the error incurred by the proposed numerical method as a function of the spatial and temporal resolution. These tests are performed using a circular vortex patch (with circulation Γ) that is initially filled with heavy particles, in the absence of gravity. The initial distributions of both vorticity and particle concentration have a Gaussian form, with radial length scale σ. Nondimensionalization is performed using σ and Γ/σ as characteristic length and velocity scales, respectively. Because we wish to focus on the effect of the particles in these validation tests, viscous diffusion of the fluid phase is neglected, although the viscous drag of the particles is retained. This approximation is consistent with a limit of high flow Reynolds number.

Preliminary calculations show that in the absence of gravity, the vorticity and particle concentration fields remain axisymmetric throughout the computation. The two-dimensional Lagrangian vorticity method (hereafter referred to as LVM) computations are compared

against the results of a one-dimensional axisymmetric calculation based on an Eulerian finite-difference method (hereafter referred to as FDM). For axisymmetric swirling flow without viscous diffusion and gravity force and with no radial fluid velocity, the governing equations for the FDM calculations become

$$\frac{\partial \omega}{\partial t} = \frac{1}{r}\frac{\partial}{\partial r}\left[\frac{rcE(v_\theta - u_\theta)}{\mathrm{St}}\right], \tag{23}$$

$$\frac{\partial c}{\partial t} = -\frac{1}{r}\frac{\partial}{\partial r}(rcV_r), \tag{24}$$

$$\frac{dv_r}{dt} = \frac{v_\theta^2}{r} - \frac{Ev_r}{\mathrm{St}}, \tag{25}$$

$$\frac{dv_\theta}{dt} = -\frac{v_r v_\theta}{r} - \frac{E}{\mathrm{St}}(v_\theta - u_\theta), \tag{26}$$

where $E \equiv 1 + 0.15\,\mathrm{Re}_p^{0.687}$. The first term on the right-hand side of (25) and (26) comes from the centrifugal force acting on the particles. (These terms are derived when the vector equation (6) is written in terms of its polar components.) The fluid azimuthal velocity u_θ is obtained by inverting the vorticity definition to yield

$$u_\theta(r,t) = \frac{1}{r}\int_0^r r'\omega(r',t)\,dr'. \tag{27}$$

The FDM calculations solve the vorticity transport equation (23) and the particle concentration equation (24) on a uniform grid using centered finite-differences. The particle momentum equations (25)–(26) are solved on Lagrangian particle control points, in which linear interpolation is employed to relate variables defined on the particle and fluid control points. The fluid velocity u_θ is obtained by solving (27) using the standard trapezoidal method. Time evolution is performed using the MacCormack scheme [35], and both the temporal and spatial resolution are sufficiently fine that the FDM solutions can be regarded as "exact."

Numerical results for vorticity and particle concentration within a vortex patch with maximum initial particle concentration (at the center of the vortex patch) of $c_{\max} = 0.3$ are given in Figs. 1 and 2, in which the solid lines represent the FDM results and the symbols represent the LVM results at different times. The LVM calculations are performed using 1027 fluid control points and 5000 particle control points. These fluid and particle control points are initially arranged in 15 and 41 concentric circles, respectively, in a circular area with the radius of 2.5σ. The time step was held fixed at $\Delta t = 0.1$. The radii of both the fluid and particle control points were set adaptively by calculating the average separation distance between the control point and its four closest control points (of the same class) and then multiplying by an "overlap" factor of 2. The particle velocity is initially set to be identical to the fluid velocity at the location occupied by the particle.

Two sets of LVM computations for the vortex patch flow are reported in Figs. 2a and 2b; for one, the averaging length scale α_m in (21) is set equal to zero and for the other, α_m is set equal to the particle radius δ_m. The vorticity results for these two cases are nearly identical, and results for the case with $\alpha_m = 0$ are shown in Fig. 1. Vorticity profiles at all times later than the last time shown in Fig. 1 are practically identical to the lowest curve. The concentration values for the two LVM calculations exhibit small differences after a long time as the concentration profile becomes increasingly peaked. For both concentration and

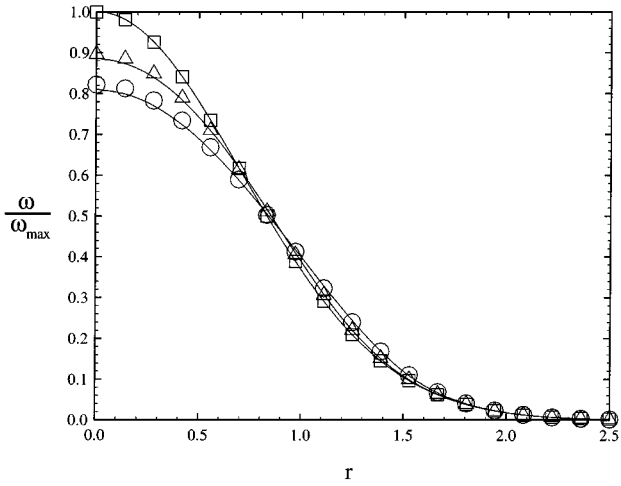

FIG. 1. Variation of vorticity ω with radius r for a Gaussian vortex patch flow filled with particles for $\mathrm{St} = 1$ and $c_{\max} = 0.3$. The axisymmetric one-dimensional FDM computational results are represented by a solid line and the two-dimensional LVM results are represented by □, Δ, and ◯ for times $t = 0$, 20, and 60, respectively. The results are normalized by the initial vorticity at the vortex center.

vorticity modification, the LVM computations are generally found to compare well with the FDM solutions, with the exception of a slight smoothing of the concentration profile for the LVM case with $\alpha_m = \delta_m$ after a long time.

The time variation of the vorticity profiles shows that particle dispersion significantly reduces the vorticity within the patch. This vorticity reduction results from the negative vorticity generated by the particles as they move radially outward under the action of the centrifugal force. As the particle concentration in the vortex core region decreases, the vorticity reduction rate slows down and the vorticity eventually approaches an asymptotic profile. For instance, the computed maximum vorticity in Fig. 1 at time $t = 200$ differs only by about 4% from that shown at time $t = 60$.

The particles evolve into a thin, high-concentration band that translates radially outward from the vortex core. The width of this particle band becomes thinner and the maximum particle concentration becomes larger with time. The nature of the particle evolution observed in Fig. 2 is similar to that reported by Druzhinin [37], who obtained an analytical solution for the particle concentration wave for small Stokes numbers. Despite the high value of the particle concentration in this outward-traveling wave, the effect of the particles on the fluid vorticity seems to be negligible after they are ejected from the vortex core. This observation is due to the fact that the propagation speed of this particle wave decreases steadily with time, so that the difference between the fluid and particle velocities becomes very small.

It is desirable to examine the variation of these results as different numerical parameters are varied. Results for the effect of averaging length scale α_m on the vorticity and concentration profiles are shown in Figs. 3a and 3b, respectively, for cases with $\alpha_m = 0$, δ_m, and $2\delta_m$ at time $t = 120$. The averaging length scale is observed in Fig. 3a to have only a slight effect on the vorticity modification. However, the concentration peak in Fig. 3b is observed to become smoothed as α_m is increased, resulting in a 15% difference in maximum value of particle concentration between cases with $\alpha_m = 0$ and $\alpha_m = 2\delta_m$. It is noted that the moving

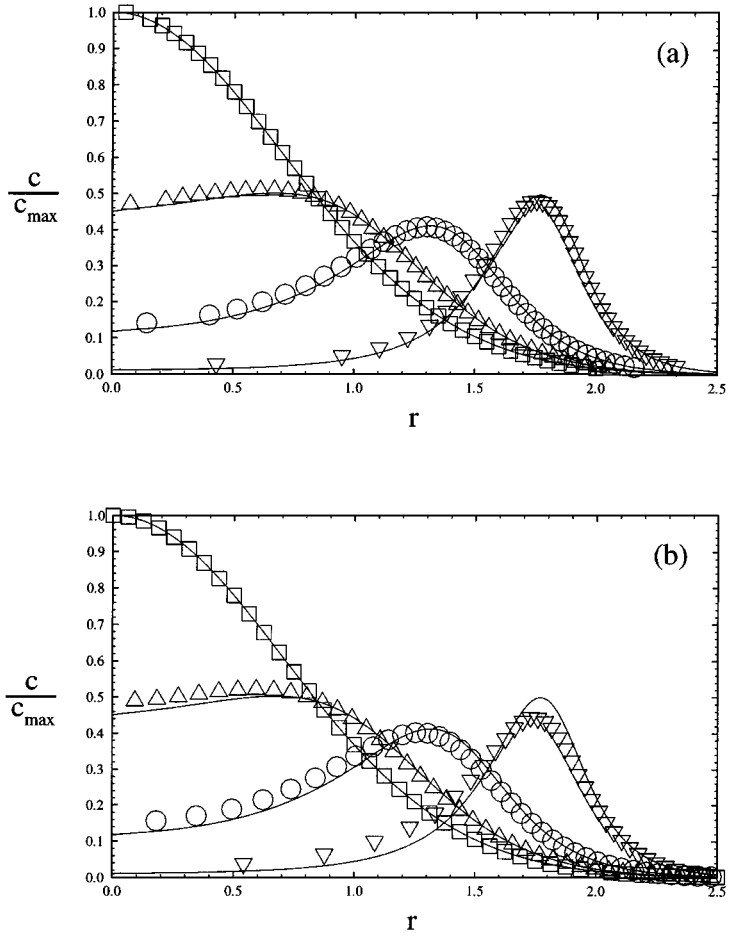

FIG. 2. Variation of particle concentration c with radius r for a Gaussian vortex patch filled with particles, for $\mathrm{St} = 1$ and $c_{\max} = 0.3$. The axisymmetric one-dimensional FDM computational results are represented by a solid line and the two-dimensional LVM results are represented by the □, Δ, ◯, and ∇ for times $t = 0$, 20, 80, and 140, respectively. The results are normalized by the initial value of particle concentration at the vortex center. Plots are given for cases with two different values of the averaging length scale α_m: (a) $\alpha_m = 0$ and (b) $\alpha_m = \delta_m$.

least-square differentiation method has a certain amount of implicit filtering, which might explain why both the vortex patch flow and numerous other flow calculations are found to yield smooth vorticity and concentration fields even when no explicit averaging is used (i.e., $\alpha_m = 0$).

The LVM computations reported in Figs. 1 and 2 were also repeated with different numbers of particle control points and different time steps, and the "error" is obtained by the difference between the LVM and FDM results. The averaging length scale α_m is set to zero in these parameter tests in order to eliminate the concentration smoothing effect. Since the error in vorticity is consistently less than the error in particle concentration, by at least one order of magnitude, we focus on concentration error in these tests. The error in c, evaluated at $r = 0$, is plotted versus time in Fig. 4 for LVM computations with $M = 5000$ particle control points and five different time steps. The error decreases monotonically with decrease in Δt; however, as Δt becomes smaller than about $\Delta t = 0.1$, the error becomes

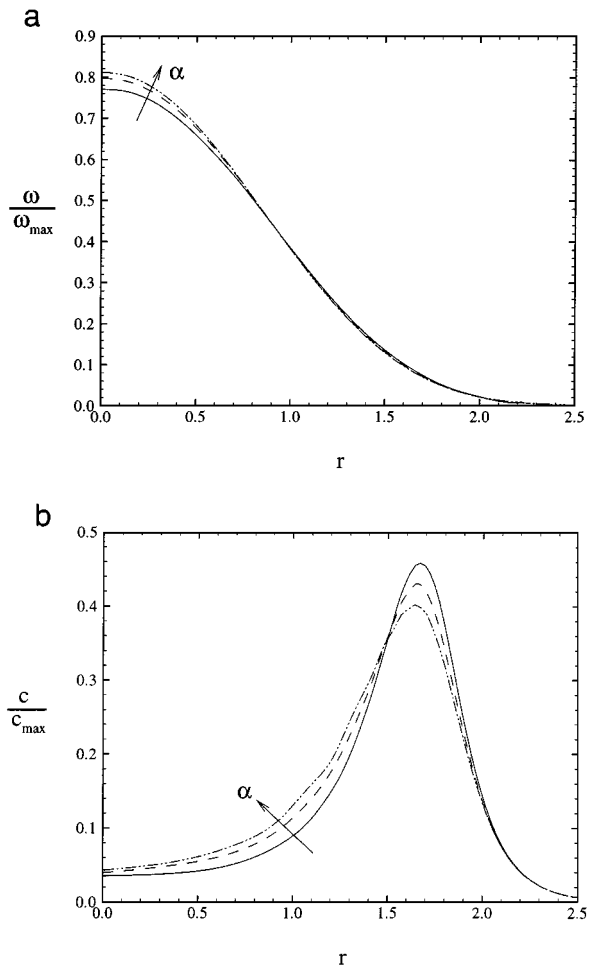

FIG. 3. Plots illustrating the effect of the averaging length scale α_m on the evolution of (a) vorticity and (b) particle concentration for a Gaussian vortex patch filled with particles, with $\mathrm{St} = 1$ and $c_{\max} = 0.3$. LVM results are given for cases with $\alpha_m = 0$ (solid curve), $\alpha_m = \delta_m$ (dashed curve), and $\alpha_m = 2\delta_m$ (dash–dotted–dotted curve). The time step is fixed at $\Delta t = 0.1$, the number of particles is fixed at 5000, and the plot is given at time $t = 120$.

increasingly controlled by the spatial resolution and does not exhibit significant further decrease for smaller Δt.

The error in particle concentration also decreases with increasing number of particle control points, as shown in Fig. 5 for computations with $\Delta t = 0.1$ and four different numbers of particle control points. This spatial resolution error results principally from the approximation of the divergence of the average particle velocity in (7) with the moving least-square method. The error of the moving least-square method is proportional to the square of average separation distance between the control points [34]. Good results (with error less than 2% of the FDM results) are obtained for the vortex patch with 5000 particle control points, which corresponds to a distance of 0.04 between the particle control points at the beginning of the calculation.

For a vortex patch filled with particles with a small Stokes number (i.e., $\mathrm{St} \ll 1$), the motion of the flow in the center region can be approximated by a rigid-body rotation, and the following asymptotic approximations (valid to leading order in St) for the vorticity and

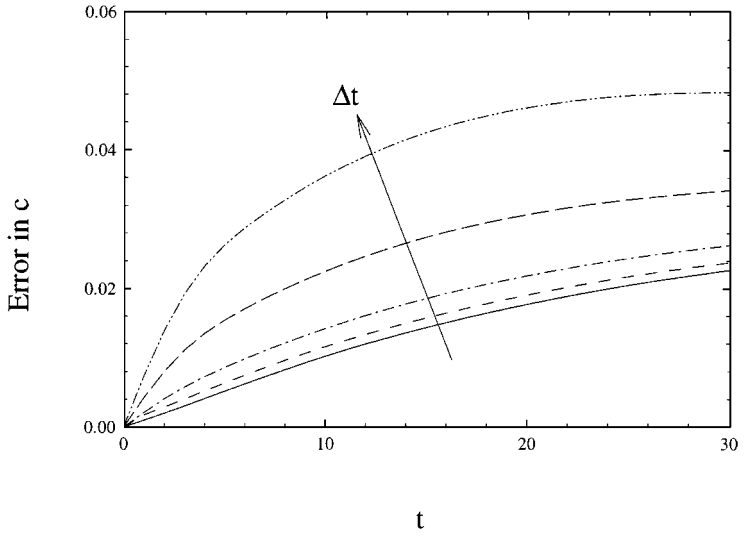

FIG. 4. Plot illustrating the effect of time step on the maximum error in particle concentration (at $r = 0$) for the two-dimensional LVM computations with a Gaussian vortex patch filled with particles. The solid, dashed, dash–dotted, long-dashed, and dash–dotted–dotted curves are for runs with $\Delta t = 0.05, 0.1, 0.2, 0.5$, and 1.0, respectively. Other parameters are fixed as follows: $M = 5000$, $\mathrm{St} = 1$, $c_{\max} = 0.3$, $\alpha_m = 0$.

particle concentration at the center of the vortex patch can be derived [38]

$$\frac{d\omega_0}{dt} \cong -\frac{c_0\omega_0^3 St}{2(1+c_0)}, \qquad \frac{dc_0}{dt} \cong -\frac{\omega_0^2 c_0 St}{2}, \tag{28}$$

where $\omega_0 = \omega(0, t)$ and $c_0 = c(0, t)$ are vorticity and concentration at the center of the vortex patch. The system (28) is solved numerically by the fourth-order Runge–Kutta method. The

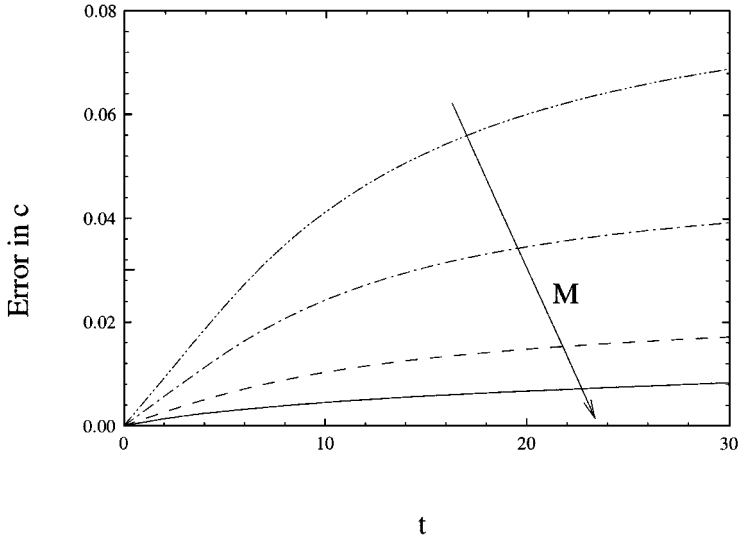

FIG. 5. Plot illustrating the effect of the number of particle control points M on the maximum error in particle concentration (at $r = 0$) for the two-dimensional LVM computations with a Gaussian vortex patch flow filled with particles. The solid, dashed, dash–dotted, and dash–dotted–dotted curves are for runs with $M = 10000$, 5000, 2000, and 1000, respectively. Other parameters are fixed as follows: $\Delta t = 0.1$, $\mathrm{St} = 1$, $c_{\max} = 0.3$, $\alpha_m = 0$.

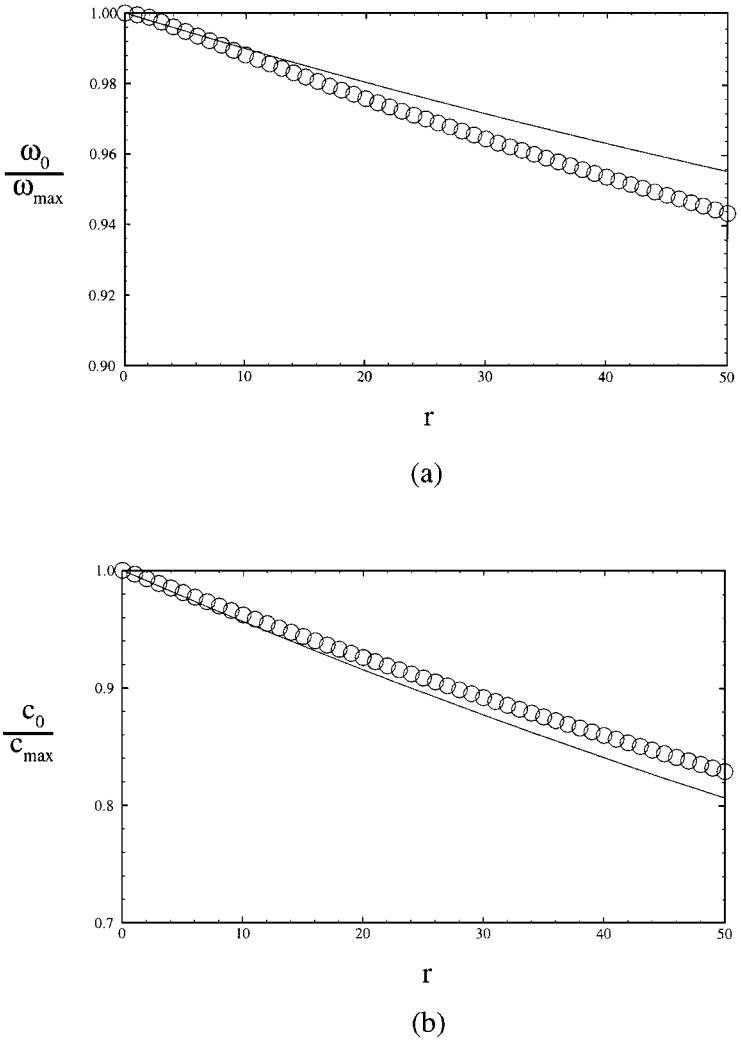

FIG. 6. Time variation of (a) vorticity and (b) particle concentration at the vortex patch center for a case with $\mathrm{St} = 0.1$ and $c_{\max} = 0.3$. The solid line represents the small St asymptotic solution and ◯ represents the two-dimensional LVM results.

time variation of the vorticity and the particle concentration for a case with with $\mathrm{St} = 0.1$ and $c_{\max} = 0.3$ is shown in Figs. 6a and 6b. The asymptotic expressions (28) show good agreement with the LVM results for a time period of about 3 or 4 times $1/\mathrm{St}$, but gradually begin to deviate from the computational predictions over longer times. This behavior is not unusual for asymptotic solutions of this type, and it should be possible to extend this good agreement for longer time intervals by further reducing the Stokes number.

5. EXAMPLE COMPUTATION FOR A FLOW DOMINATED BY PARTICLE-INDUCED VORTICITY

As noted in the Introduction, one of the advantages of vorticity-based methods is that fluid control points need only be introduced in regions where there is significant vorticity.

However, particle dispersion may cause the particle control points to separate from the fluid control points by large distances, so that it is no longer possible for the existing fluid control points to absorb the particle-induced vorticity source. This situation is remedied with the use of an adaptive scheme for fluid control point generation, which is described in Section 3.

In the current section, we report the results of a calculation that demonstrates the capability of the fluid control point insertion scheme for resolving the particle-induced vorticity. In this calculation, the flow is again initialized as a Gaussian vortex patch filled with particles (with an initial Gaussian concentration profile), but we now admit the presence of a downward gravitational field. The particle behavior under the combined effects of the gravitational field and the vortex-induced flow depends principally on the value of the Froude number. When the Froude number is small enough, the particles initially located within the vortex patch fall through the patch, forming after sufficient time an elongated vorticity wake field trailing the particles.

In the calculation reported here, the dimensionless parameters that control the two- phase flow are set as $\mathrm{Fr} = 0.2$, $c_{\max} = 0.3$, and $\mathrm{St} = 1$. The averaging length scale α_m is set equal to the element radius δ_m. The positions of the fluid control points at three different times are shown in Fig. 7. Initially, both the fluid and the particle control points are placed within a circular region (Fig. 7a). As time proceeds, the particles fall through the vortex patch, deforming and elongating the vortex patch in the negative y direction (Fig. 7b). As the particles leave the initial vortex patch, new fluid control points are generated in the vicinity of the falling particles, such that by the time shown in Fig. 7c, a long trail of these newly generated fluid control points is found lying between the falling particles and the initial vortex patch.

The spatial resolution of the fluid control points inserted in this manner can be controlled by adjusting the maximum number N_L of particles in the smallest size box. Since in the current computations it is desired that the mean separation distance between the inserted

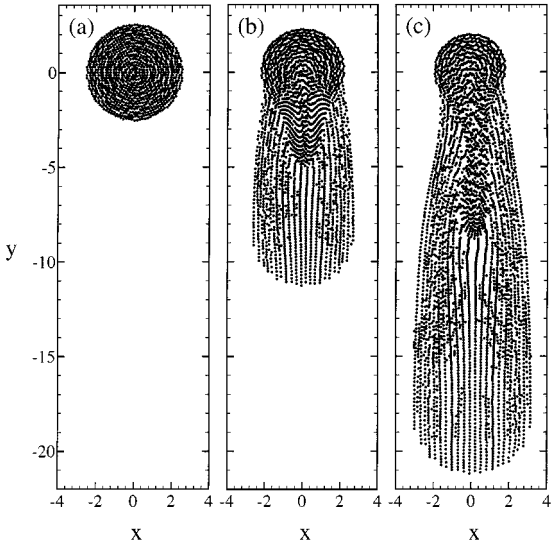

FIG. 7. Positions of the fluid control points in a flow initialized as a Gaussian vortex patch filled with particles for a case with $\mathrm{Fr} = 0.2$, $\mathrm{St} = 1$, and $c_{\max} = 0.3$ at times (a) $t = 0$, (b) $t = 2$, and (c) $t = 4$.

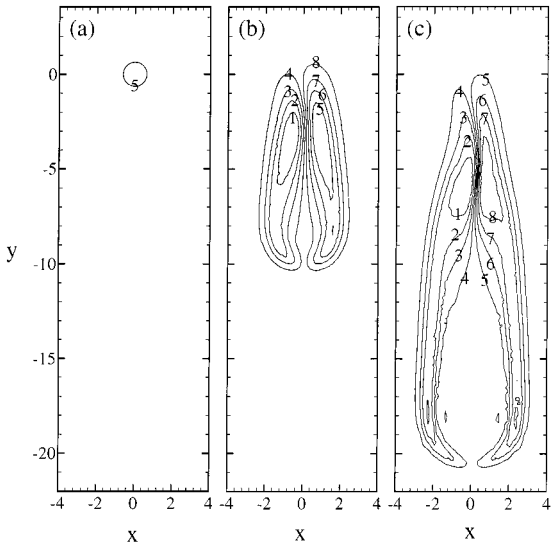

FIG. 8. Vorticity contour plots for the flow described in the caption to Fig. 7 at times (a) $t = 0$, (b) $t = 2$, and (c) $t = 4$. The vorticity increment between each level is 0.27 with the minimum value -1.2 corresponding to the curve numbered 1.

fluid control points be similar to that for the initial fluid control points within the vortex patch, the value of N_L is set equal to the initial number of particle control points divided by the initial number of fluid control points.

Contour plots of the vorticity field within the falling particle patch and in its wake are shown at three different times in Fig. 8. For this Froude number, the gravity effects are much stronger than the inertial force within the original vortex patch. The vortex patch is therefore quickly absorbed into the wake of the falling particles, within which the vorticity is much higher (by a factor of nearly four) than within the original vortex patch.

The wake-like form of the vorticity field in Fig. 8 is indicative of a downward jet of fluid trailing the particles. The effect of this downward jet is apparent in the V-like indentation of the region occupied by the particle control points as shown in Fig. 9. Similarly, in the contour plots of the particle concentration in Fig. 10, the downward jet generated by the particle-induced vorticity causes the particles to collapse into a thin arc, where the middle part of the arc (near $x = 0$) falls more rapidly than the ends of the arc.

6. TWO-PHASE PLANE MIXING LAYER

In this section, we examine the effect of particles on the fluid vorticity in a periodic plane mixing layer, with Gaussian initial vorticity and concentration profiles, using the Lagrangian vorticity method described in Section 3. The computations are performed by following the evolution of a single period of the flow with wavelength λ in the streamwise (x) direction. The velocity field induced by the vorticity outside of the computational domain $0 < x < \lambda$ is taken into account by adding a sufficient number of periods of the vorticity field on each side of the computational domain in calculation of the Biot–Savart integral. Tests of the velocity calculation show that with five periods included on each side, the maximum error in velocity is less than 5% of the exact result obtained by treating the images of the vortex blobs as point vortices [40]. The velocity induced by neighboring periods requires

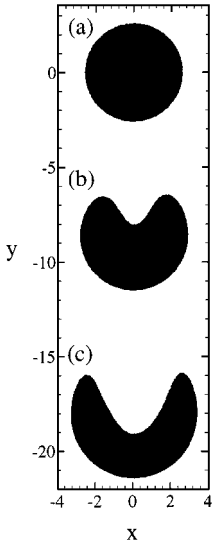

FIG. 9. The evolution of the particle control points with time for the flow described in the caption to Fig. 7 at times (a) $t = 0$, (b) $t = 2$, and (c) $t = 4$.

relatively little time to compute, since nearly all of the points can be treated indirectly using the multipole acceleration method.

The initial distributions of vorticity and particle concentration across the mixing layer have the form

$$\omega(\vec{\mathbf{x}}) = -\frac{\Delta U}{\sqrt{\pi}\sigma} \exp(-y^2/\sigma^2), \qquad c(\vec{\mathbf{x}}) = c_{\max} \exp(-y^2/\sigma^2), \tag{29}$$

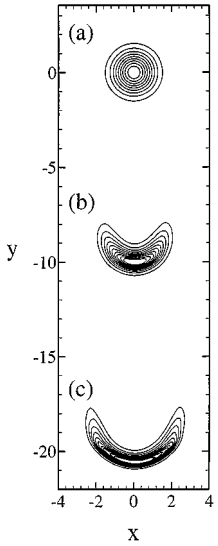

FIG. 10. Contours of the particle concentration for the flow described in the caption to Fig. 7 at times (a) $t = 0$, (b) $t = 2$, and (c) $t = 4$. The concentration increment between each level is 0.11 with the minimum value 0.12 corresponding to the outermost curve.

where ΔU is the velocity difference across the layer and σ is the Gaussian core radius. ΔU and σ are chosen as the characteristic velocity and length scales, respectively, used in writing the problem in dimensionless form. In the computations, the vorticity field of the mixing layer is discretized initially using 4100 fluid control points and the particulate phase is discretized using 9150 particle control points. The two sets of control points are initially uniformly placed in a region of width 2.5σ, and then the locations of the control points are randomly perturbed by up to 30% of their initial separation distances prior to the start of the computations. An initial random perturbation of this sort is generally advisable in computations using the Lagrangian vorticity method in order to avoid alignment of control points later in the computation, which increases the matrix condition number for the moving least-square differentiation scheme.

Both the fluid and particle control point positions and the vorticity and particle concentration fields are perturbed by a sinusoidal wave with displacement amplitude equal to 0.05λ. This perturbation induces the instability and the roll-up of the shear layer. In all the computations reported here, the wave length is chosen as $\lambda = 13.2\sigma$, which corresponds to the wave with the maximum growth rate from the single-phase linear stability theory [40].

The effect of the particles on the flow field is examined in both a high Reynolds number case (such that diffusion of the vorticity field is neglected) and in a low Reynolds number case ($\mathrm{Re} = 100$). The parameters used in the computations are the Stokes number ($\mathrm{St} = 1$) and the initial maximum particle concentration ($c_{\max} = 0.3$). In both cases, we compare the results obtained with the one-way coupling approximation to the full two-way coupling results. The averaging length scale α_m is set equal to the element radius δ_m for all cases. Both the vorticity and the particle concentration contours are obtained by interpolation using a Delauney triangularization of the fluid and particle control points, which in regions of the flow where the resolution of the concentration and vorticity fields are sparse gives the plots a somewhat jagged appearance.

The evolution of the mixing layer, both with and without the influence of particles, consists of growth of the initial perturbation wave with time and eventual roll-up into a spiral vortex structure. This spiral vortex structure exhibits a concentrated eddy at the center of the period and two stretched vorticity braids connecting to the two neighboring eddies. This structure is evident, for instance, in the vorticity contour plots for the high Reynolds number case shown in Fig. 11 for the case with one-way coupling. When two-way coupling is employed in the simulation (Fig. 12), the eddy at the center of the spiral structure is much weaker due to the vorticity decrease associated with dispersion of particles from the central vortex by the centrifugal force. For instance, at time $t = 30$, the vorticity at the eddy center is about 0.47 in the case with two-way coupling and 0.56 in the case with one-way coupling.

The particles are only very slowly dispersed from the vorticity spirals, since the centrifugal force at large radius is much weaker than within the center vortex, so the vorticity within the spirals does not show strong decay. In the two-way coupling case with high Reynolds number, the vorticity within the spiral braids is observed to first increase with time and then decrease as the particles move through. For instance, in the case shown in Fig. 12, the maximum vorticity within the braids increases to 0.98 at time $t = 30$, whereas the maximum vorticity is initially only 0.56. This increase is caused by the addition of vorticity from the high-concentration particle bands that are dispersed from the central eddy and pass through the vorticity spirals. In addition to augmenting the vorticity within the spiraling braids, the high-concentration bands also produce negative vorticity, leading to the development of regions of weak vorticity of the opposite sign to the initial vorticity in Fig. 12b.

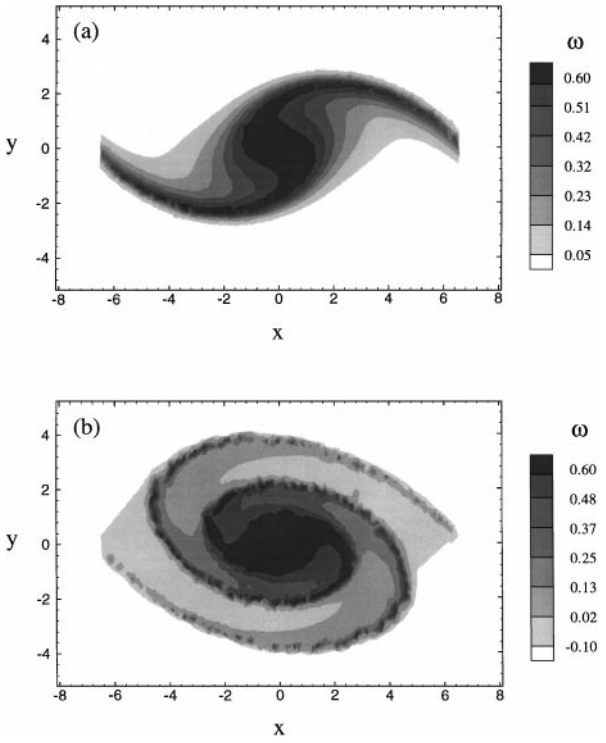

FIG. 11. Vorticity contours for a high Reynolds number two-phase mixing layer with $\mathrm{St} = 1$ and $c_{\max} = 0.3$ at times (a) $t = 15$ and (b) $t = 35$, with one-way coupling.

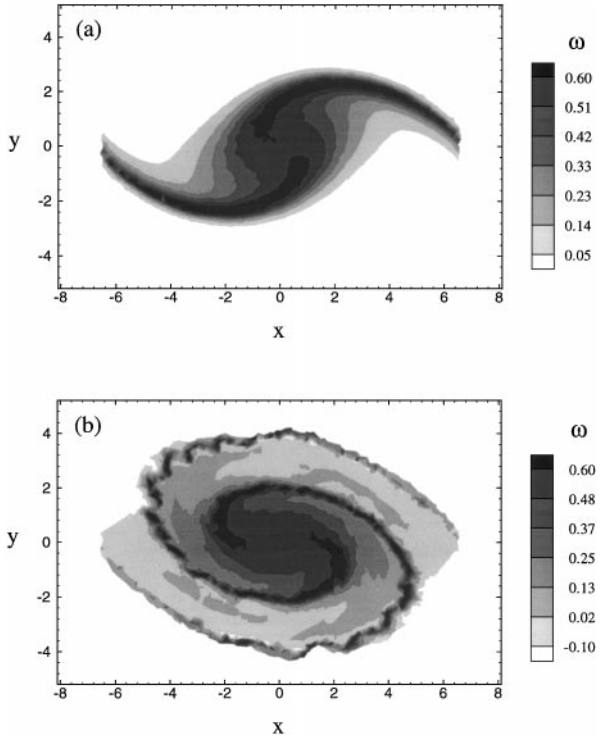

FIG. 12. Vorticity contours for the flow described in the caption to Fig. 11 at times (a) $t = 15$ and (b) $t = 35$, with two-way coupling.

The vorticity spirals for the two-way coupling case exhibit a pronounced Kelvin–Helmholtz instability that causes them to become increasingly wavy with time, as shown in Fig. 12b. The spiral arms in the one-way coupling case also exhibit small oscillations (Fig. 11b), but the oscillation amplitude is less than in the two-way coupling case. This difference may be due either to the increased strength of the spiral arms for the two-way coupling case or to the perturbations due to vorticity generated by the high-concentration particle bands.

Both the one-way coupling and the two-way-coupling results indicate that the particles tend to move outward under the centrifugal force induced by the central vortex and collect in bands near the outer edge of the vortex structure. This behavior is consistent with the results of several previous studies of particle dispersion in mixing layers [6, 9]. Figure 13 shows the two-way coupling result for particle dispersion in a high Reynolds number flow. The particle concentration near the outer edge of the vortex increases with time, such that a narrow band with high particle concentration eventually develops, as shown in the contour plot of the particle concentration field in Fig. 13b. It can be seen from Fig. 13b that the particle concentration has two peaks within the high-concentration particle band. The maximum particle concentration is observed to be as high as 7 times the initial value in the two-way coupling computations.

The two-phase mixing layer computations were repeated for a low Reynolds number case with $\mathrm{Re} = 100$. The effect of viscosity is to diffuse vorticity in both the spiral braids and in the central vortex, such that eventually the braids nearly disappear (in the one-way coupling

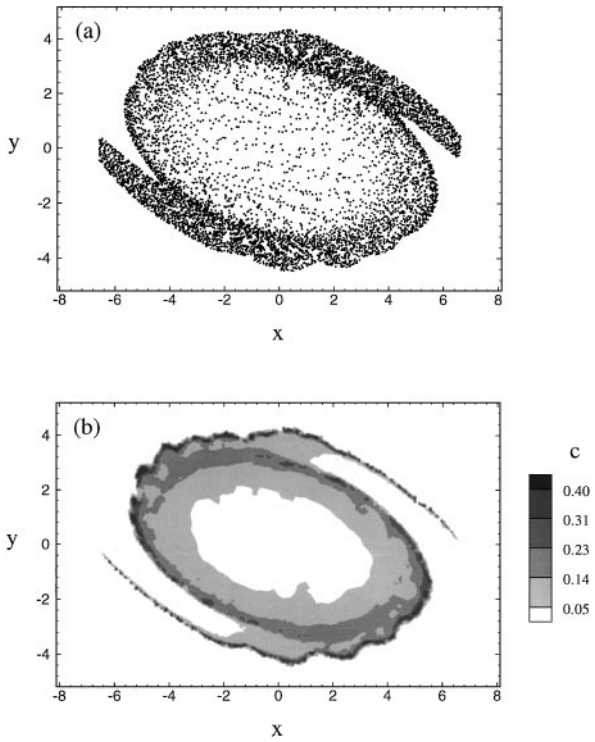

FIG. 13. (a) The locations of the particle control points and (b) contours of particle concentration for the flow described in the caption to Fig. 11 at time $t = 35$.

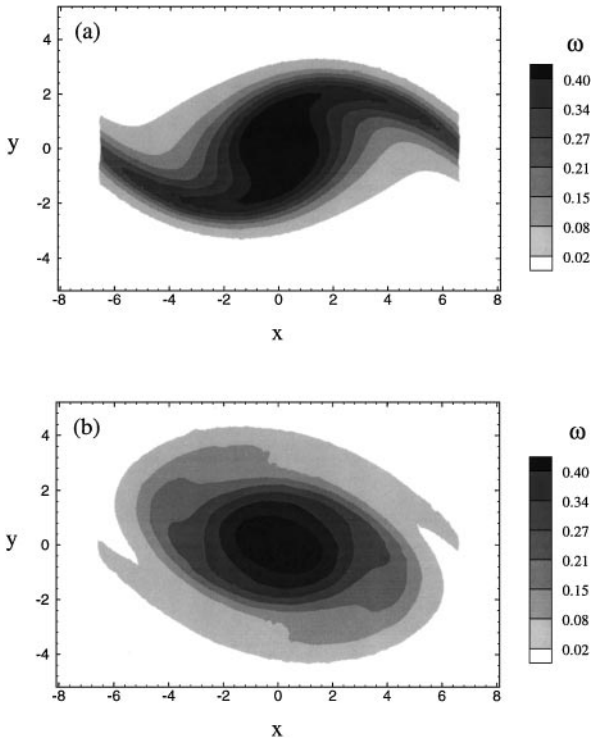

FIG. 14. Vorticity contours for a viscous two-phase mixing layer with $\mathrm{St} = 1$, $c_{\max} = 0.3$, and $\mathrm{Re} = 100$ at times (a) $t = 15$ and (b) $t = 35$, with one-way coupling.

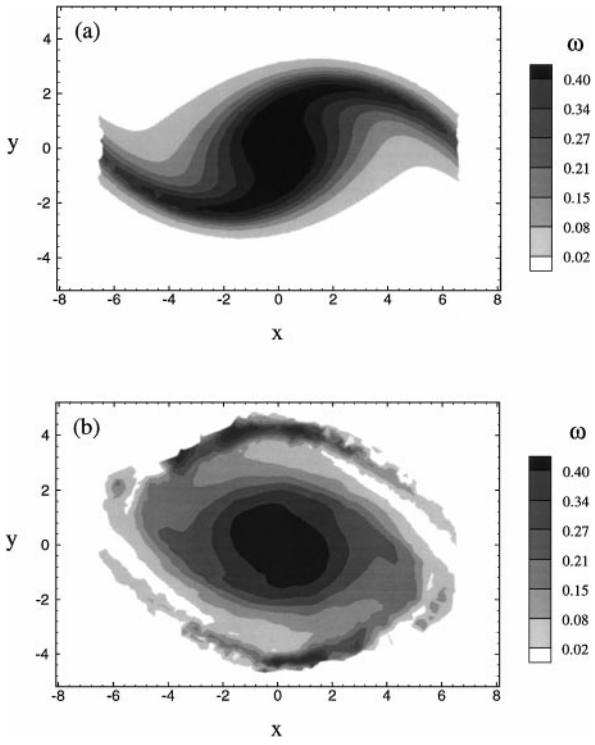

FIG. 15. Vorticity contours for the flow described in the caption to Fig. 14 at times (a) $t = 15$ and (b) $t = 35$, with two-way coupling.

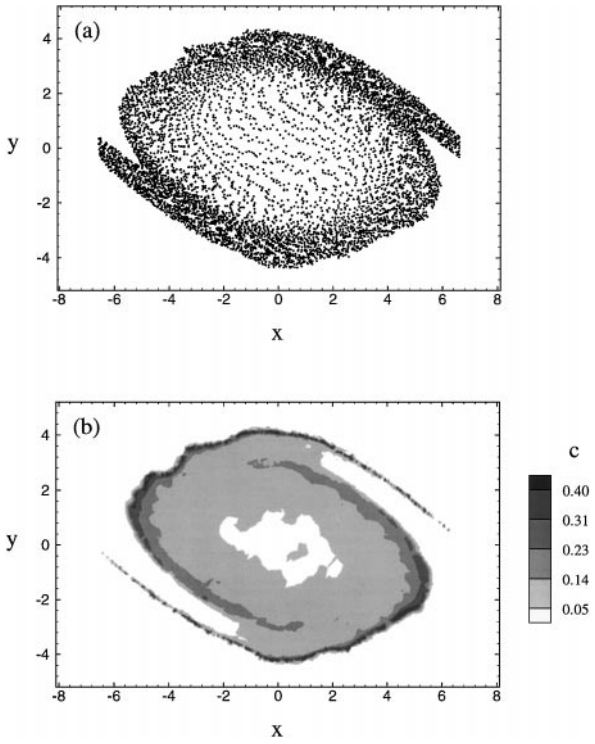

FIG. 16. (a) The locations of the particle control points and (b) contours of particle concentration for the flow described in the caption to Fig. 14 at time $t = 35$.

case) and an elliptic vortex patch is formed at the center. The vorticity within this center eddy diffuses outward with time under the effect of the viscous diffusion. Vorticity contours at the same two times are shown for the one-way and two-way coupling cases in Figs. 14 and 15, respectively. The largest effect of two-way coupling is the appearance of two strong vorticity spirals near the location of the high-concentration particle bands (Fig. 15b), both above and below the central vortex. The spiral braids in the one-way coupling case have nearly completely diffused away by the time shown in Fig. 14b, which suggests that the vorticity within the strong spiral braids observed in the two-way coupling case (Fig. 15b) is generated by the particles and does not arise from the initial mixing layer vorticity.

The particle dispersion in the case with $\mathrm{Re} = 100$ is qualitatively similar to that in the high Reynolds number case. The particle control points and the particle concentration contours are shown in Fig. 16, which again indicates that the particles tend to move away from the center vortex and concentrate in narrow bands near the outer region of the vortex structure.

7. CONCLUSIONS

In this paper, a new approach for computation of two-phase flows is introduced which combines aspects of the two-fluid and Lagrangian particle approaches. In this approach, representative particles are advected by the flow, with velocity determined by solution of the momentum equation for an individual particle. A moving averaging procedure is employed to compute the volume-averaged particle velocity and contact force fields. The average particle velocity is used to evolve the particle concentration directly on the Lagrangian particle

control points. The product of the average contact force and the particle concentration gives the particle force acting on the fluid.

This solution approach for the particle phase can be implemented with any common solution method for the fluid phase, using either a velocity–pressure or a vorticity–velocity formulation. Both the particle concentration and contact force are obtained on the Lagrangian particle control points without the need for a grid covering the flow field, and the approach avoids the need for particle "clustering" often used in the Lagrangian particle approach. The current paper employs a Lagrangian vortex method to evolve the fluid phase, such that a separate set of fluid control points are introduced on which the vorticity is evolved by solution of the vorticity transport equation. The vorticity changes on a fluid control point both because of viscous diffusion and because of vorticity generation by the nonconservative body force induced by the particles. The fluid control points are advected with the sum of the local fluid velocity and an additional "diffusion velocity" that accounts for the spread of vorticity support due to diffusion. A fast integration method is used to obtain the fluid velocity at both the fluid and the particle control point locations, which is based on sorting the fluid and the particle control points into tree-like box structures and applying the multipole expansion. A method for differentiation across the two sets of control points is described using the moving least-square procedure. The solution procedure for the fluid phase is given only for a two-dimensional flow in this paper, but extension of this procedure to three dimensions requires only slight modification of the Biot–Savart integral, addition of the vortex stretching term in the vorticity transport equation, and terms in the z-direction for the polynomial fit (15) used in the least-square differentiation.

The numerical method is validated by a series of computations with a Gaussian vortex patch filled with particles. The results show that negative vorticity is generated by the particles as they are advected away from the vortex center due to the centrifugal force, which results in reduction in the vorticity magnitude at the vortex center. The numerical results are in good agreement with the results obtained by a one-dimensional Eulerian finite-difference method. The computed vorticity and particle concentration at the center of the vortex patch also agree well with Druzhinin's asymptotic approximation for small Stokes numbers and short times.

A method for fluid control point generation near the particle locations is proposed in the paper using an adaptive box sorting algorithm. A fluid control point generation scheme is necessary since particle dispersion can lead to situations where there are few or no fluid control points near the particles to absorb the particle-induced vorticity. The fluid control point generation scheme is demonstrated in a calculation of a particle cloud falling under gravity, which exhibits a long wake of vorticity trailing the falling particle cloud.

Computations are also presented that examine the effect of two-way coupling in two-phase plane mixing layer flow. In agreement with previous studies, the particles are found to move away from the center of the vortex spiral and accumulate in a narrow band with high particle concentration that wraps around the central vortex. The particle-induced vorticity source decreases the vorticity within the central eddy as the vorticity layer rolls up into a spiral structure. Within the spiraling vorticity braids, the two-way phase coupling leads to the formation of regions where the vorticity is increased or decreased compared to its ambient value on either side of the braid. The particle-induced vorticity is also observed to enhance the development of secondary Kelvin–Holmholtz instability within the vorticity spiral braids.

APPENDIX A: DERIVATION OF PARTICLE-INDUCED VORTICITY SOURCE

The local average force $\vec{\mathbf{P}}$ acting on a single particle in the vicinity of a point $\vec{\mathbf{x}}$ at time t is given by

$$\vec{\mathbf{P}} = \left(\rho_p V_p U^2/L\right)\vec{\mathbf{F}}, \tag{A1}$$

where $\vec{\mathbf{F}}(\vec{\mathbf{x}}, t)$ is the dimensionless average force defined in (5), V_p is the volume of a single particle, and U and L are the characteristic velocity and length scales of the fluid flow. We now let N denote the number of particles per unit volume of the mixture, so that the product $V_p N$ is equal to the local average $\langle a \rangle$ of the indicator function $a(\vec{\mathbf{x}}, t)$ introduced in Section 2. The particle force is opposed by a force of equal magnitude acting on the fluid phase, which appears as a nonconservative body force on the fluid [13]. The value of the fluid body force $\vec{\mathbf{b}}$ per unit volume of the mixture is given by the product of the particle number density N times the local average force $-\vec{\mathbf{P}}$ acting on the fluid from a single particle, or

$$\vec{\mathbf{b}} = -N\left(\rho_p V_p U^2/L\right)\vec{\mathbf{F}}. \tag{A2}$$

The particle mass concentration, defined in Section 2, is given simply by $\rho_p N V_p$, so that the dimensionless particle concentration c is $\rho_p N V_p/\rho_f$. Dividing by $\rho_f U^2/L$, we can thus write (A2) as

$$\frac{\vec{\mathbf{b}}}{\rho_f U^2/L} = -c\vec{\mathbf{F}}. \tag{A3}$$

The expression (A3) yields the dimensionless fluid body force per unit volume, the curl of which provides a source term that appears on the right-hand side of the vorticity transport equation (8).

APPENDIX B: ACCELERATED VELOCITY CALCULATION METHOD

Direct calculation of the induced velocity of N control points requires an amount of work of $O(N^2)$, which can become excessive for large N. In the current paper, we utilize an adaptive multipole acceleration scheme [41] for calculation of the fluid velocity at both fluid and particle control points. In this method, the fluid control points are sorted into boxes having a tree-like structure, and a multipole expansion is used to approximate the induced velocity of control points in boxes that are sufficiently far away from the point where the velocity is desired. The velocity of control points closer than some cutoff distance is computed directly. The construction of this box hierarchy is performed in the manner described in Section 3, its primary features being that the box sorting is completely adaptive and each box within a given generation contains approximately the same number of control points.

For each "smallest box" of the tree-like family, two interaction lists are generated, corresponding to boxes for which the velocity calculation is performed "directly" or "indirectly" (i.e., using the multipole expansion). These box interaction lists are determined based on a critical value of the distance between the vorticity "source" points and the "target" points, at which the velocity is desired. The critical distance depends both on the allowable error and the order of terms retained in the multipole expansion. For each smallest-size "target"

box ℓ, we first scan over the set of largest-size "source" boxes n_L to examine whether the minimum distance between points in box ℓ and those in each of the largest-size boxes n_L is greater than the cutoff distance. If it is, the box n_L is placed on the "indirect" interaction list of box ℓ. If the box separation distance is not greater than the cutoff distance, this procedure is repeated with the offspring of box n_L, and so on. If this ratio is not greater than the cutoff value for one of the smallest-size source boxes n_k, the source box n_k is placed on the "direct" interaction list of the target box ℓ. The "target" and the "source" points in this procedure may consist of either the same set of points (as when determining velocity on fluid control points) or different sets of points (as when determining velocity on particle control points).

For a point P with location $\vec{\mathbf{x}}_p$, the fluid velocity is given by the sum

$$\vec{\mathbf{u}}(\vec{\mathbf{x}}_p, t) = \vec{\mathbf{u}}_{\text{dir}} + \frac{1}{2\pi} \sum_{\ell=1}^{L} \sum_{m=0}^{\infty} \sum_{n=0}^{\infty} \frac{(-1)^{m+n}}{m!n!} \mathbf{J}_{\ell,mn} \frac{\partial^{m+n}}{\partial x^m \partial y^n} \left(\frac{\vec{\mathbf{k}} \times \vec{\mathbf{r}}}{r^2} \right), \tag{B1}$$

where the first term on the right-hand side, $\vec{\mathbf{u}}_{\text{dir}}$, represents the portion of the velocity contributed from the control points contained in the boxes that are on the direct interaction list of the smallest-size box containing point P and the second term is the portion of the velocity contributed from the control points contained in the boxes that are on the indirect interaction list. This second term in (B1) is obtained as a sum over the L boxes on the indirect list index, where $\vec{r} \equiv \hat{\vec{x}}_\ell - \vec{x}_p$, $r \equiv |\vec{\mathbf{r}}|$, and $\hat{\vec{x}}_\ell$ is the location of the mass center of box ℓ. The symbol $\boldsymbol{J}_{\ell,mn}$ denotes the "moment" of box ℓ and is defined by

$$\boldsymbol{J}_{\ell,mn} = \sum_{q=1}^{N_\ell} \Omega_q (x_q - \hat{x}_\ell)^m (y_q - \hat{y}_\ell)^n, \tag{B2}$$

where N_ℓ is the number of control points in box ℓ, $\hat{x}_\ell$ and $\hat{y}_\ell$ are the x- and y-components of the box center location $\hat{\vec{x}}_\ell$, and Ω_q is the amplitude of the qth vorticity element (given by (14)). The moment $\boldsymbol{J}_{\ell,mn}$ of box ℓ is independent of the point P at which the velocity is computed, which allows this term to be computed once and stored at each time step.

Direct calculation of the derivative in (B1) can be time consuming for large values of m and n. However, these derivatives can be rapidly computed from recurrence relations, such that only the first derivatives need to be computed directly. Letting α and β be the x- and y-components of $\vec{\mathbf{k}} \times \vec{\mathbf{r}}/r^2$, respectively, and using the identities

$$\frac{\partial}{\partial x}(r^2\beta) = 1, \qquad -\frac{\partial}{\partial y}(r^2\alpha) = 1, \tag{B3}$$

we can derive the following recurrence relations (valid for $m \geq 2$) for the derivatives in (B1):

$$\begin{aligned}
r^2 \frac{\partial^m \beta}{\partial x^m} + 2mx \frac{\partial^{m-1} \beta}{\partial x^{m-1}} + m(m-1) \frac{\partial^{m-2} \beta}{\partial x^{m-2}} &= 0, \\
r^2 \frac{\partial^m \alpha}{\partial y^m} + 2my \frac{\partial^{m-1} \alpha}{\partial y^{m-1}} + m(m-1) \frac{\partial^{m-2} \alpha}{\partial y^{m-2}} &= 0, \\
r^2 \frac{\partial^m}{\partial x^m} \left(\frac{\partial \beta}{\partial y} \right) + 2y \frac{\partial^m \beta}{\partial x^m} + 2mx \frac{\partial^{m-1}}{\partial x^{m-1}} \left(\frac{\partial \beta}{\partial y} \right) + m(m-1) \frac{\partial^{m-2}}{\partial x^{m-2}} \left(\frac{\partial \beta}{\partial y} \right) &= 0, \\
r^2 \frac{\partial^m}{\partial y^m} \left(\frac{\partial \alpha}{\partial x} \right) + 2x \frac{\partial^m \alpha}{\partial y^m} + 2my \frac{\partial^{m-1}}{\partial y^{m-1}} \left(\frac{\partial \alpha}{\partial x} \right) + m(m-1) \frac{\partial^{m-2}}{\partial y^{m-2}} \left(\frac{\partial \alpha}{\partial x} \right) &= 0.
\end{aligned} \tag{B4}$$

From the fact that α and β are harmonic functions, another set of recurrence relations follows:

$$\begin{aligned}
&\frac{\partial^m \alpha}{\partial x^m} = (-1)^{m/2}\frac{\partial^m \alpha}{\partial y^m}, \quad \frac{\partial^m \beta}{\partial y^m} = (-1)^{m/2}\frac{\partial^m \beta}{\partial x^m}, && \text{for even } m \\
&\frac{\partial^m \alpha}{\partial x^m} = (-1)^{(m-1)/2}\frac{\partial^{m-1}}{\partial y^{m-1}}\left(\frac{\partial \alpha}{\partial x}\right), \quad \frac{\partial^m \beta}{\partial y^m} = (-1)^{(m-1)/2}\frac{\partial^{m-1}}{\partial x^{m-1}}\left(\frac{\partial \beta}{\partial y}\right), && \text{for odd } m.
\end{aligned} \tag{B5}$$

Together (B4) and (B5) are sufficient to determine all the derivatives in (B1) for $m \geq 2$.

The speed of the computation depends on both the number of boxes on the interaction lists and the number of terms included in the multipole expansion. The fewer control points contained in boxes on the direct interaction list and the fewer terms included in the expansions, the faster the calculation. The number of boxes on the direct interaction list depends on the cutoff value d_{crit} of the target–source box separation distance. The smaller the value of d_{crit}, the shorter the direct interaction list. On the other hand, the error associated with truncation of the multipole expansions increases as d_{crit} decreases, thus requiring more terms to be retained to obtain solutions of the desired accuracy.

An optimization procedure is reported by Winckelmans *et al.* [42], in which the critical distance d_{crit} is evaluated based on a modified version of the theoretical upper bound for the absolute error in the multipole expansion derived by Salmon and Warren [43]. A numerical test of this upper bound for a variety of flow types has been performed, which indicates that the true error is typically about an order of magnitude lower than indicated by the theoretical bound. The maximum number of control points N_L in the smallest-size box is determined simply by comparing the time T_{dir} required to directly compute the induced velocity between two points and the time T_h required to compute the induced velocity at one point by a single box using the multipole expansion method with terms through order h. The multipole expansion method is efficient only if $T_h < N_L T_{\text{dir}}$, which yields the lower bound

$$N_L > T_h / T_{\text{dir}}. \tag{B6}$$

Both the highest order h in the multipole expansion and the maximum absolute error from any given box must be specified prior to the computation.

ACKNOWLEDGMENTS

Research support was provided by a grant from the Central Investment Fund for Research Enhancement of the University of Iowa. Computer time was provided by a grant from the San Diego Supercomputing Center.

REFERENCES

1. C. T. Crowe, R. A. Gore, and T. R. Troutt, Particle dispersion by coherent structures in free shear flows, *Particle Sci. Technol.* **3**, 149 (1985).
2. J. N. Chung and T. R. Troutt, Simulation of particle dispersion in an axisymmetric jet, *J. Fluid Mech.* **186**, 199 (1988).
3. R. Chein and J. N. Chung, Simulation of particle dispersion in a two-dimensional mixing layer, *AIChE J.* **34**, 946 (1988).
4. K. D. Squires and J. K. Eaton, Preferential concentration of particles by turbulence, *Phys. Fluids A* **3**, 1169 (1991).

5. L. Tang, F. Wen, Y. Yang, C. T. Crowe, J. N. Chung, and T. R. Troutt, Self-organizing particle dispersion mechanism in a plane wake, *Phys. Fluids A* **4**, 2244 (1992).
6. F. Wen, N. Kamalu, J. N. Chung, C. T. Crowe, and T. R. Troutt, Particle dispersion by vortex structures in plane mixing layers, *J. Fluid Eng.* **114**, 657 (1992).
7. C. T. Crowe, J. N. Chung, and T. R. Troutt, Particle dispersion by organized turbulent structures, in *Particulate Two-Phase Flow*, edited by M. C. Roco (1993), Chap. 18, p. 626.
8. S. Elghobashi and G. C. Truesdell, Direct simulation of particle dispersion in a decaying turbulence, *J. Fluid Mech.* **242**, 655 (1992).
9. J. E. Martin and E. Meiburg, The accumulation and dispersion of heavy particles in forced two-dimensional mixing layers. I. The fundamental and subharmonic cases, *Phys. Fluids* **6**, 1116 (1994).
10. S. Elghobashi, On predicting particle-laden turbulent flows, *Appl. Sci. Res.* **52**, 309 (1994).
11. S. A. Drew, Averaged field equations for two-phase media, *Stud. Appl. Math.* **L**, 133 (1971).
12. S. L. Soo, *Particulates and Continuum: Multiphase Fluid Dynamics* (Hemisphere, New York, 1989).
13. C. T. Crowe, T. R. Troutt, and J. N. Chung, Numerical models for two-phase turbulent flows, *Ann. Rev. Fluid Mech.* **28**, 11 (1996).
14. M. Sommerfeld, Modeling of particle wall collisions in confined gas-particle flows, *Int. J. Multiphase Flow* **18**, 905 (1992).
15. D. E. Stock, Particle dispersion in flowing gases: 1994 Freeman Scholar lecture, *J. Fluids Eng.* **118**, 4 (1996).
16. A. A. Mostafa and H. C. Mongia, On the interaction of particles and turbulent fluid flow, *Int. J. Heat Mass Transfer* **31**, 2063 (1988).
17. K. D. Squires and J. K. Eaton, Particle response and turbulence modification in isotropic turbulence, *Phys. Fluids A* **2**, 1191 (1990).
18. S. Elghobashi and G. C. Truesdell, On the two-way interaction between homogeneous turbulence and dispersed particles. I. Turbulence modulation, *Phys. Fluids A* **5**, 1790 (1993).
19. Y. Ogami and T. Akamatsu, Viscous flow simulation using the discrete vortex model—The diffusion velocity method, *Comput. Fluids* **19**, 433 (1991).
20. S. N. Kempka and J. H. Strickland, *A Method to Simulate Viscous Diffusion of Vorticity by Convective Transport of Vortices at a Non-solenoidal Velocity*, Sandia Nat. Lab. Tech. Rept., SAND93-1763 (1993).
21. M. R. Maxey and J. J. Riley, Equation of motion for a small rigid sphere in a non-uniform flow, *Phys. Fluids* **24**, 883 (1983).
22. P. G. Saffman, The lift on a small sphere in a slow shear flow, *J. Fluid Mech.* **22**, 385 (1965).
23. P. G. Saffman, Corrigendum to "The lift force on a small sphere in a slow shear flow," *J. Fluid Mech.* **31**, 624 (1968).
24. D. S. Dandy and H. A. Dwyer, A sphere in shear flow at finite Reynolds number: effect of shear on particle lift, drag, and heat transfer, *J. Fluid Mech.* **216**, 381 (1990).
25. R. Mei, An approximate expression for the shear lift force on spherical particles at finite particle Reynolds number, *Int. J. Multiphase Flow* **18**, 145 (1992).
26. R. Clift, J. R. Gracs, and M. E. Weber, *Bubbles, Drops and Particles* (Academic Press, London, 1978), p. 111.
27. A. Leonard, Vortex methods for flow simulation, *J. Comput. Phys.* **37**, 785 (1980).
28. A. Leonard, Computing three-dimensional incompressible flows with vortex elements, *Ann. Rev. Fluid Mech.* **17**, 523 (1985).
29. J. T. Beale and A. Majda, Vortex methods. I. Convergence in three dimensions, *Math. Comput.* **39**, 1 (1982).
30. C. Anderson and C. Greengard, On vortex methods, *SIAM J. Numer. Anal.* **22**, 413 (1985).
31. G. S. Winckelmans and A. Leonard, Contributions to vortex particle method for the computation of three-dimensional incompressible unsteady flows, *J. Comput. Phys.* **109**, 247 (1993).
32. J. T. Beale, On the accuracy of vortex methods at large times, in *Proc. Workshop on Comput. Fluid Dyn. Reacting Gas Flows.* (I. M. A., University of Minnesota, 1986).
33. J. S. Marshall and J. R. Grant, Penetration of a blade into a vortex core: vorticity response and unsteady blade forces, *J. Fluid Mech.* **103**, 83 (1996).

34. J. S. Marshall and J. R. Grant, A Lagrangian vortex method for viscous axisymmetric fluid flows, with and without swirl, *J. Comput. Phys.* **138**, 302 (1997).
35. R. Peyret and T. D. Taylor, *Computational Methods for Fluid Flow* (Springer-Verlag, New York, 1990), p. 45.
36. L. Greengard and V. Rokhlin, A fast algorithm for particle simulations, *J. Comput. Phys.* **73**, 325 (1987).
37. O. A. Druzhinin, Concentration waves and flow modification in a particles-laden circular vortex, *Phys. Fluids* **6**, 3276 (1994).
38. O. A. Druzhinin, Dynamics of concentration and vorticity modification in a cellular flow laden with solid heavy particles, *Phys. Fluids* **7**, 2132 (1995).
39. Y. Nakamura, A. Leonard, and P. Spalart, Vortex simulation of an inviscid shear layer, AIAA Paper, No. 82-0948 (1992).
40. A. Michalke, On the inviscid instability of the hyperbolic-tangent velocity profile, *J. Fluid Mech.* **19**, 543 (1964).
41. L. Greengard and V. Rokhlin, A fast algorithm for particle simulations, *J. Comput. Phys.* **73**, 325 (1987).
42. G. S. Winckelmans, Three-dimensional vortex particle and panel methods: Fast treecode solvers with active error control for arbitrary distributions/geometries, in *Proc. of the Forum on the Vortex Methods for Engineering Applications, Albuquerque, NM* (1995), p. 25.
43. J. K. Salmon and M. S. Warren, Skeletons from the treecode closet, *J. Comput. Phys.* **111**, 136 (1994).